

Time-dependent formulation of the two-dimensional model of resonant electron collisions with diatomic molecules and interpretation of the vibrational excitation cross sections

Martin Váňa* and Karel Houfek†

*Institute of Theoretical Physics, Faculty of Mathematics and Physics, Charles University in Prague,
V Holešovičkách 2, 180 00 Praha 8, Czech Republic*

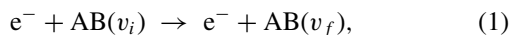
(Received 10 January 2017; published 23 February 2017)

A two-dimensional model of the resonant electron-molecule collision processes with one nuclear and one electronic degree of freedom introduced by K. Houfek, T. N. Rescigno, and C. W. McCurdy [Phys. Rev. A **73**, 032721 (2006)] is reformulated within the time-dependent framework and solved numerically using the finite-element method with the discrete variable representation basis, the exterior complex scaling method, and the generalized Crank-Nicolson method. On this model we illustrate how the time-dependent calculations can provide deep insight into the origin of oscillatory structures in the vibrational excitation cross sections if one evaluates the cross sections not only at sufficiently large time to obtain the final cross sections, but also at several characteristic times which are given by the evolution of the system. It is shown that all details of these structures, especially asymmetrical peaks, can be understood as quantum interference of several experimentally indistinguishable processes separated in time due to a resonant capture of the electron and the subsequent vibrational motion of the negative molecular ion. Numerical results are presented for the N₂-like, NO-like, and F₂-like models and compared with ones obtained within the time-independent approach and within the local complex potential approximation.

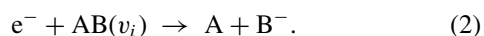
DOI: [10.1103/PhysRevA.95.022714](https://doi.org/10.1103/PhysRevA.95.022714)

I. INTRODUCTION

In the paper [1], a simple two-dimensional model of resonant electron collisions with diatomic molecules was introduced to study in detail validity of various approximate approaches for treating the nuclear dynamics that plays an important role during these collisions, especially if one is interested in processes such as vibrational excitation (VE) of a molecule by an electron impact



and dissociative electron attachment (DA)



The model has two degrees of freedom, the internuclear distance R and the electron distance r , with the potential energy chosen in such a way to reproduce qualitatively the complex potential energy curve of a certain negative molecular ion when fixed-nuclei calculations are performed. Three models for the molecules N₂, NO, and F₂ were constructed in [1] and [2]. The validity of the local complex potential (LCP) approximation to the nuclear dynamics for these three systems was discussed in [1] and the more elaborate nonlocal theory of the nuclear dynamics [3] was considered later in [2]. It was shown that the nonlocal theory is much more accurate than the local complex potential approximation and works well for all three studied systems.

In papers [1] and [2], the time-independent approach was used to solve the two-dimensional (2D) problem and to calculate the cross sections of the processes (1) and (2) within the full model and also within the LCP and nonlocal approximations. In this paper we solve the 2D problem using

the time-dependent approach to get deeper insight into the dynamics of the electron-molecule collisions and compare results with the time-dependent LCP approximation. The time-dependent calculations within the nonlocal theory are much more involved [3,4] and not considered in this paper because we focus here mainly on the correct description of time evolution of the 2D system and on the interpretation of the VE cross sections based on this evolution.

We should note that time-dependent calculations for the same two-dimensional model were performed also by Shandilya *et al.* [5] but their cross sections disagree with the previous results of the time-independent calculations. For example, the structures in the VE cross sections are much narrower than should be (see Fig. 7). We should stress here that both the time-dependent and time-independent approaches in the quantum mechanics are equivalent for systems with the time-independent Hamiltonian. If a given problem is in both approaches formulated consistently and solved properly the final results (the cross sections in our case) must be the same as is demonstrated in this paper. Therefore, we disagree with the claim of Shandilya *et al.* in [5] that “these features [narrower oscillatory structures in the VE cross sections] could be genuine and fresh experiments with better resolution are required to settle this issue.” Furthermore, the 2D model introduced in [1] was not developed and constructed for direct comparison with experiments although the cross sections obtained from the 2D model resemble the experimental ones.

The results of the time-dependent calculations enabled us to discuss in details the origin of structures in the VE cross sections. In the literature, see, e.g., [3,6] and references therein, the cross sections are usually obtained within the time-independent framework and an explanation of the origin of these features is very often provided only within the *boomerang* model by Herzenberg *et al.* [7–9]. This simple model assumes that the boomerang structures in the cross sections result from the interference of two processes, a direct

*vana_martin@post.cz

†houfek@mbox.troja.mff.cuni.cz

decay of the resonant state of the negative molecular ion without nuclear motion and a time-delayed release of the electron after one vibrational motion of the nuclei. But such interference leads to a very regular interference pattern in the VE cross sections and for a full explanation of details of these structures, especially of highly asymmetrical peaks, it is necessary to consider interference of several processes due to repeated vibrational motion. Within the time-independent picture the detailed discussion of the resulting cross sections can be sometimes quite complicated [10]. Here we propose a simple method of how to determine the origin of these features which is based on comparing the cross sections with contributions integrated up to a certain distinctive time given by the dynamics of the system, in this case after each period of the vibrational motion of the negative molecular ion, as discussed in Sec. VIII.

As in papers [1] and [2] we give all relations and values in tables and figures in atomic units, in which $\hbar = m_e = 1$. Internuclear distances are given in units of the Bohr radius $a_0 = 5.291\,772 \times 10^{-11}$ m, cross sections in units of $a_0^2 = 2.800\,285 \times 10^{-21}$ m², and energies in units of hartrees, where 1 hartree = 4.359 748 $\times 10^{-18}$ J. The atomic unit of time is 1 a.u. = 2.418 884 $\times 10^{-17}$ s.

II. TWO-DIMENSIONAL MODEL

In this section we give a brief description of the two-dimensional model as it was introduced by Houfek, Rescigno, and McCurdy in [1] and [2]. The Hamiltonian of this model reads

$$H = -\frac{1}{2\mu} \frac{\partial^2}{\partial R^2} - \frac{1}{2} \frac{\partial^2}{\partial r^2} + V(R, r), \quad (3)$$

where μ denotes the reduced molecular mass and $V(R, r)$ is the model potential

$$V(R, r) = V_0(R) + \frac{l(l+1)}{2r^2} + V_{\text{int}}(R, r), \quad (4)$$

where l denotes the electron angular momentum chosen to correspond to the electron partial wave with the largest contribution to the cross section in a real system, $V_0(R)$ is the potential energy describing vibrational motion of the neutral molecule when the electron is at large distances, i.e.,

$$V_0(R) = \lim_{r \rightarrow \infty} V(R, r), \quad (5)$$

and $V_{\text{int}}(R, r)$ is the interaction part of the potential given by two functions $\lambda(R)$ and $\alpha(R)$ as

$$V_{\text{int}}(R, r) = \lambda(R)e^{-\alpha(R)r^2}, \quad (6)$$

chosen to obtain various models each similar to a different real system.

The molecular potential is approximated by the Morse potential

$$V_0(R) = D_0(e^{-2\alpha_0(R-R_0)} - 2e^{-\alpha_0(R-R_0)}), \quad (7)$$

where D_0 controls the depth of the potential well, α_0 its width, and R_0 its position. For three models introduced in [1] and [2] it is not necessary to consider α as a function of R ; thus

TABLE I. Constants and potential parameters for N₂⁻, NO⁻, and F₂-like models, given in atomic units, so that the resulting potential is in hartrees.

constant	N ₂	NO	F ₂
μ	12 766.36	13 614.16	17 315.99
l	2 (<i>d</i> wave)	1 (<i>p</i> wave)	1 (<i>p</i> wave)
D_0	0.75102	0.2363	0.0598
α_0	1.15350	1.5710	1.5161
R_0	2.01943	2.1570	2.6906
λ_∞	6.21066	6.3670	18.8490
λ_1	1.05708	5.0000	3.2130
R_λ	-27.9833	2.0843	1.8320
λ_c	5.38022	6.0500	18.1450
R_c	2.40500	2.2850	2.5950
α_c	0.40000	1.0000	3.0000

we put

$$\alpha(R) = \alpha_c. \quad (8)$$

At last we specify the function $\lambda(R)$, which was chosen in such a way to have a bound electronic state for large internuclear distances R and a resonant state for small R . For all models investigated in this paper it has the following form:

$$\lambda(R) = \lambda_\infty + \frac{\lambda_0}{1 + e^{\lambda_1(R-R_\lambda)}}, \quad (9)$$

$$\lambda_0 = (\lambda_c - \lambda_\infty)(1 + e^{\lambda_1(R_c - R_\lambda)}). \quad (10)$$

The parameter λ_∞ controls the potential as $R \rightarrow \infty$; the parameter λ_c determines the value of $\lambda(R)$ at the crossing point R_c of the potential curve $V_0(R)$ and the potential energy curve $E_{\text{res}}(R)$ [see Eq. (41) below] corresponding to the internuclear distance where the resonant state becomes a bound state. See Table I for the values of the parameters.

III. TIME-DEPENDENT APPROACH

The time-independent description of resonant collisions within the two-dimensional model described above was given in [1]. Here we introduce an equivalent time-dependent formulation of the collision processes.

The unperturbed Hamiltonians in the asymptotic regions of the vibrational excitation (VE) and dissociative attachment (DA) channels are

$$H_0^{\text{VE}} = -\frac{1}{2} \frac{\partial^2}{\partial r^2} + \frac{l(l+1)}{2r^2} - \frac{1}{2\mu} \frac{\partial^2}{\partial R^2} + V_0(R), \quad (11)$$

$$H_0^{\text{DA}} = -\frac{1}{2} \frac{\partial^2}{\partial r^2} - \frac{1}{2\mu} \frac{\partial^2}{\partial R^2} + V_b(r), \quad (12)$$

where the potential $V_b(r)$ is given by the limit

$$V_b(r) = \lim_{R \rightarrow \infty} V(R, r). \quad (13)$$

The first Hamiltonian H_0^{VE} describes the molecule in a certain vibrational state and a free electron far from the molecule. The second Hamiltonian H_0^{DA} describes the electron attached to one component of the molecule and the components far from each other.

For convenience, as in [2], we define the unperturbed energy-normalized ($E = k^2/2$) electronic continuum states with the angular momentum l as

$$\mathcal{J}_k^l(r) = \sqrt{\frac{2k}{\pi}} r j_l(kr), \quad (14)$$

where j_l is the spherical Bessel function of the first kind, and the unperturbed energy-normalized ($E = K^2/2\mu$) molecular-anion continuum state as

$$\mathcal{E}_K(R) = \sqrt{\frac{2\mu}{\pi K}} \sin(KR). \quad (15)$$

The energy-normalized incident eigenstate of H_0^{VE} with the total energy $E = E_{v_i} + k_i^2/2$ is then given by

$$\varphi_{v_i}^{\text{in}}(E, R, r) = \chi_{v_i}(R) \mathcal{J}_{k_i}^l(r), \quad (16)$$

where $\chi_{v_i}(R)$ is the initial vibrational state of the molecule, the solution of

$$\left(-\frac{1}{2\mu} \frac{\partial^2}{\partial R^2} + V_0(R) \right) \chi_{v_i}(R) = E_{v_i} \chi_{v_i}(R). \quad (17)$$

The energy-normalized outgoing eigenstate for the final vibrational state v_f is

$$\varphi_{v_f}^{\text{out}}(E, R, r) = \chi_{v_f}(R) \mathcal{J}_{k_f}^l(r) \quad (18)$$

and the outgoing eigenstate in the DA channel with the total energy $E = E_b + K^2/2\mu$ is

$$\varphi_{\text{DA}}^{\text{out}}(E, R, r) = \mathcal{E}_K(R) \phi_b(r), \quad (19)$$

where $\phi_b(r)$ denotes the electronic bound state in the potential $V_b(r)$ (we assume there is only one such state which is true for models investigated in this paper).

As an initial state of the time evolution we take the molecule in a certain initial vibrational state $\chi_{v_i}(R)$ and the incoming electron described by a Gaussian wave packet of the width σ placed at r_0 in the asymptotic region, i.e.,

$$\Psi_{v_i}^{\text{in}}(R, r) = \frac{1}{(\pi\sigma^2)^{\frac{1}{4}}} \chi_{v_i}(R) e^{-\frac{(r-r_0)^2}{2\sigma^2} - ip_0 r}, \quad (20)$$

where p_0 denotes the mean momentum of the incoming electron. The elements of the S matrix are defined in terms of the asymptotic eigenstates (16), (18), and (19) of the channel Hamiltonians (11) and (12). For a given channel the eigenstates form a complete basis. In the initial vibrational excitation channel we can thus expand the wave function into the basis (16) as

$$\Psi_{v_i}^{\text{in}}(R, r) = \int_0^\infty \eta_{v_i}^{\text{in}}(\varepsilon) \chi_{v_i}(R) \mathcal{J}_k^l(r) d\varepsilon, \quad (21)$$

where k denotes the electron momentum given by $k = \sqrt{2\varepsilon} = \sqrt{2(E - E_{v_i})}$ with E_{v_i} being the energy of the initial vibrational state and the coefficients $\eta_{v_i}^{\text{in}}(E)$ are

$$\eta_{v_i}^{\text{in}}(E) = \int_0^\infty \int_0^\infty \varphi_{v_i}^{\text{in}}(E, R, r)^* \Psi_{v_i}^{\text{in}}(R, r) dr dR. \quad (22)$$

The propagation of the wave function is given by application of the unitary evolution operator

$$\psi(t + t_0) = U(t) \psi(t_0) = e^{-iHt} \psi(t_0). \quad (23)$$

The evolved wave function will be outgoing into all accessible channels and we need to calculate the S matrix from these outgoing waves. For this purpose we have tested three methods for the evaluation of the S -matrix elements.

The first is the correlation function approach described by Tannor and Weeks [11]. Here we give only a brief overview and necessary formulas. The complete derivation by using the spectral method or from the relations of completeness may be found in [11]. The method is based on the integration over time of the overlap of the evolved wave function with a test function placed in a channel of interest. In the vibrational excitation channels we assume the test function to be a product of the final vibrational state $\chi_{v_f}(R)$ and an outgoing Gaussian wave packet in the electronic degree of freedom

$$\Phi_{v_f}^{\text{out}}(R, r) = \frac{1}{(\pi\sigma^2)^{\frac{1}{4}}} \chi_{v_f}(R) e^{-\frac{(r-r_0)^2}{2\sigma^2} + iq_0 r}. \quad (24)$$

In the dissociative attachment channel we assume the test function to be a product of the attached electron bound state $\phi_b(r)$ and an outgoing Gaussian wave packet

$$\Phi_{\text{DA}}^{\text{out}}(R, r) = \frac{1}{(\pi\sigma^2)^{\frac{1}{4}}} \phi_b(r) e^{-\frac{(r-R_0)^2}{2\sigma^2} + iQ_0 R}. \quad (25)$$

As mentioned above, the elements of the S matrix are defined in terms of the asymptotic eigenstates (18) and (19); thus decompositions of the test functions similar to (22) can be utilized. If we introduce the correlation function as an overlap of the evolved wave function with the test function in one of the possible channels

$$C_\beta(t) = \int_0^\infty \int_0^\infty [\Phi_\beta^{\text{out}}(R, r)]^* \psi(R, r, t) dr dR, \quad (26)$$

where β stands for v_f or DA, then the S matrix for both processes can be obtained from

$$S_{v_i \rightarrow \beta}^{\text{T\&W}}(E) = \frac{(2\pi)^{-1}}{[\eta_\beta^{\text{out}}(E)]^* \eta_{v_i}^{\text{in}}(E)} \int_{-\infty}^\infty C_\beta(t) e^{iEt} dt, \quad (27)$$

where E is the same for all channels and it is the total energy of the system

$$E = \frac{k_i^2}{2} + E_{v_i} = \frac{k_f^2}{2} + E_{v_f} = \frac{K^2}{2\mu} + E_b. \quad (28)$$

Although the above relations provide a proper means to calculate the S -matrix elements, in practice one can encounter some numerical difficulties if the test functions are narrow and placed improperly. Since the test functions may in general contain contributions of incoming as well as outgoing waves and the eigenstates (18), (19) do not distinguish the orientation of impulse, one should place the test functions closer to the interaction region than the incident wave packet (at least in the initial channel). Therefore in the following we choose a different approach considering only the outgoing part of the test functions: however we must now place the test functions farther from the interaction region than the incident wave packet to guarantee there is no overlap with the incoming waves. The coefficients $\eta_\beta^{\text{out}}(E)$ can then be calculated as

$$\eta_\beta^{\text{out}}(E) = \int_0^\infty \int_0^\infty \tilde{\varphi}_\beta^{\text{out}}(E, R, r)^* \Phi_\beta^{\text{out}}(R, r) dr dR, \quad (29)$$

where $\tilde{\varphi}_\beta^{\text{out}}(E, R, r)$ denotes only the outgoing part of the functions (18) and (19), i.e.,

$$\tilde{\varphi}_{v_f}^{\text{out}}(E, R, r) = \chi_{v_f}(R) \sqrt{\frac{k_f}{2\pi}} r h_l^+(k_f r), \quad (30)$$

$$\tilde{\varphi}_{\text{DA}}^{\text{out}}(E, R, r) = \sqrt{\frac{\mu}{2\pi K}} e^{iKR} \phi_b(r), \quad (31)$$

where $h_l^+(k_f r)$ denotes the outgoing spherical Hankel function.

The second method for computation of the S -matrix elements is based on the previous one and can be derived simply by using the δ function at some distance r_0 or R_0 instead of the Gaussian wave packet in the test functions (24), (25). As in the previous case we consider only the outgoing part of the δ function and the corresponding coefficients then read

$$\eta_{v_f}^{\text{out}}(E) = \sqrt{\frac{k_f}{2\pi}} r_0 h_l^+(k_f r_0)^*, \quad (32)$$

$$\eta_{\text{DA}}^{\text{out}}(E) = \sqrt{\frac{\mu}{2\pi K}} e^{-iKR_0}. \quad (33)$$

The elements of the S matrix for the vibrational excitation channels are then given by

$$S_{v_i \rightarrow v_f}^\delta(E) = \frac{1}{2\pi (\eta_{v_f}^{\text{out}}(E))^* \eta_{v_i}^{\text{in}}(E)} \times \int_{-\infty}^{\infty} \int_0^{\infty} dt dR e^{iEt} \chi_{v_f}(R)^* \psi(R, r_0, t), \quad (34)$$

and for the dissociative attachment channel by

$$S_{v_i \rightarrow \text{DA}}^\delta(E) = \frac{1}{2\pi (\eta_{\text{DA}}^{\text{out}}(E))^* \eta_{v_i}^{\text{in}}(E)} \times \int_{-\infty}^{\infty} \int_0^{\infty} dt dr e^{iEt} \phi_b(r)^* \psi(R_0, r, t). \quad (35)$$

Note that the spatial integration is reduced to the channel internal degree of freedom thanks to the δ function. This is the main advantage of this approach, since it is computationally much simpler. Also note that using the original approach with full decompositions into (18) and (19) would lead to zero values of $\eta_\beta^{\text{out}}(E)$ at some energies, thus resulting in numerical instabilities.

The third method of the evaluation of the S matrix may be derived from the time-independent formulation via projection of the flux on the given final state. Again we choose the outgoing waves approach and put $\tilde{\varphi}_{v_f}^{\text{out}}(R, r)$ given by (30) as the final state in the VE channels and $\tilde{\varphi}_{\text{DA}}^{\text{out}}(R, r)$ given by (31) in the DA channel. The elements of the S matrix can be calculated from the flux at the distance r_0 , or R_0 , far enough from the interaction zone. In the VE channels we obtain

$$S_{v_i \rightarrow v_f}^{\text{F}}(E) = \frac{1}{2\eta_{v_i}^{\text{in}}(E)} \frac{1}{2i} \int_{-\infty}^{\infty} \int_0^{\infty} dt dR e^{iEt} \times \left[(\tilde{\varphi}_{v_f}^{\text{out}})^* \left(\frac{\partial \psi(t)}{\partial r} \right) - \psi^*(t) \left(\frac{\partial \tilde{\varphi}_{v_f}^{\text{out}}}{\partial r} \right) \right]_{r=r_0}, \quad (36)$$

where we have omitted the spatial arguments (R, r) of the functions in the integrand for brevity. The S -matrix element for the DA channel is given by

$$S_{v_i \rightarrow \text{DA}}^{\text{F}}(E) = \frac{1}{2\eta_{v_i}^{\text{in}}(E)} \frac{1}{2i\mu} \int_{-\infty}^{\infty} \int_0^{\infty} dt dr e^{iEt} \times \left[(\tilde{\varphi}_{\text{DA}}^{\text{out}})^* \left(\frac{\partial \psi(t)}{\partial R} \right) - \psi^*(t) \left(\frac{\partial \tilde{\varphi}_{\text{DA}}^{\text{out}}}{\partial R} \right) \right]_{R=R_0}. \quad (37)$$

Formulas for the cross sections depend on the wave function normalization [16]. Here we used the same normalization as in the paper [2]; thus we have

$$\sigma_{v_i \rightarrow \beta}(E) = \frac{4\pi^3}{k_i^2} |T_{v_i \rightarrow \beta}(E)|^2, \quad (38)$$

where β stands again for v_f or DA and the T -matrix element is related to the S -matrix element by

$$T_{v_i \rightarrow \beta}(E) = \frac{S_{v_i \rightarrow \beta}(E) - \delta_{v_i, \beta}}{2\pi i}. \quad (39)$$

IV. LOCAL COMPLEX POTENTIAL APPROXIMATION

In the paper [1] the time-independent formulation of the LCP approximation for the two-dimensional model was described and here we summarize the time-dependent formulation. The LCP approximation solves the nuclear dynamics in the complex molecular anion potential $V_{\text{res}}(R)$, defined as poles of the fixed-nuclei scattering matrix S shifted by the neutral potential $V_0(R)$. The poles may be obtained as resonance or bound energies of the electronic Hamiltonian

$$H_{\text{el}}(r; R) = -\frac{1}{2} \frac{\partial^2}{\partial r^2} + V(R, r), \quad (40)$$

which is parametrically dependent on the internuclear distance R . The complex potential $V_{\text{res}}(R)$ can be written in the form

$$V_{\text{res}}(R) = E_{\text{res}}(R) - \frac{i}{2} \Gamma(R), \quad (41)$$

where the imaginary part is expressed using the resonance width $\Gamma(R)$. The imaginary part is nonzero only in the region where $V_0(R) < E_{\text{res}}(R)$.

We assume that the molecule is in an initial vibrational state $\chi_{v_i}(R)$ and as the initial wave packet within the LCP approximation we can take the initial vibrational state modified by a square root of the resonance width (see, e.g., [3] for details)

$$\Psi_{\text{LCP}}(R, t=0) = \sqrt{\frac{\Gamma(R)}{2\pi}} \chi_{v_i}(R). \quad (42)$$

The motion of the wave packet is given by the evolution operator (23) but now with the Hamiltonian given by

$$H_{\text{LCP}}(R) = -\frac{1}{2\mu} \frac{\partial^2}{\partial R^2} + E_{\text{res}}(R) - \frac{i}{2} \Gamma(R). \quad (43)$$

The elements of the T matrix for the VE and DA processes may be expressed as [3]

$$T_{v_i \rightarrow v_f}^{\text{LCP}}(E) = \frac{1}{i} \int_0^\infty dt \int_0^\infty dR e^{iEt} \times \chi_{v_f}^*(R) \sqrt{\frac{\Gamma(R)}{2\pi}} \Psi_{\text{LCP}}(R, t), \quad (44)$$

$$T_{v_i \rightarrow \text{DA}}^{\text{LCP}}(E) = \sqrt{\frac{K}{2\pi\mu}} \lim_{R \rightarrow \infty} e^{-iKR} \int_0^\infty dt e^{iEt} \Psi_{\text{LCP}}(R, t), \quad (45)$$

and the cross sections then read

$$\sigma_{v_i \rightarrow \beta}^{\text{LCP}}(E) = \frac{4\pi^3}{k_i^2} |T_{v_i \rightarrow \beta}^{\text{LCP}}(E)|^2, \quad (46)$$

where β again stands for any of $v_f = v_0, v_1, \dots$ or DA, k_i denotes the momentum of the incoming electron, and E is the total energy of the system given by Eq. (28).

V. PROJECTION ON A DIABATIC STATE

One of the goals of this paper is comparison of the nuclear dynamics of the full two-dimensional model with the LCP approximation. In order to be able to compare not only the resulting cross sections but also the evolution of the wave packets we use a projection of the 2D wave packet on a certain electronic state to obtain a function dependent only on the internuclear distance.

The LCP approximation can be derived from the more general nonlocal theory of the nuclear dynamics of the resonant electron-molecule collisions [3] that is based on a choice of the so-called discrete electronic state and thus on separation of the electronic Hilbert space into a resonant and background part. If the projection on this discrete state is made one gets the nuclear wave function corresponding to the resonant nuclear motion. Several possibilities of how to choose the discrete state were discussed in the paper [2]. We decided to project the 2D wave packet onto the *physical choice* of the discrete state $\phi_d(R, r)$ described in [2], the energy of which is very close to the real part of the local complex potential. The detailed discussion of the nonlocal theory is out of the scope of this paper and for details we refer to the papers cited above.

The *physical choice* of the discrete state is obtained as eigenstates of the fixed-nuclei electronic Hamiltonian corresponding to the bound state for larger internuclear distances and the resonance for smaller internuclear distances. Since the discrete state must be from the $L^2(\mathbb{R})$ Hilbert space for each R the resonance eigenstates have to be smoothly suppressed for larger electronic distances. As the suppressing function we have used

$$f(r) = 1 - \frac{1}{1 - e^{-(r-r_d)}}, \quad (47)$$

where r_d is the middle point of the region where the functions are suppressed. For further use we define a projection onto the discrete state as the integration of the overlap of the two-dimensional wave function with the discrete state over the

electronic coordinate, i.e.,

$$\Psi_d(R, t) = \int_0^\infty dr \Psi(R, r, t) \phi_d^*(R, r). \quad (48)$$

The discrete state is parametrically dependent on R due to dependence of the electronic Hamiltonian (40) on the internuclear distance.

VI. NUMERICAL SOLUTION

To obtain a numerical solution of the time-dependent Schrödinger equation we use the finite elements method combined with discrete variable representation (FEM-DVR) introduced by Rescigno and McCurdy [12] for space discretization (see also [13] for further details). As basis functions on each element we use the standard Lagrange interpolation polynomials going through Gauss-Lobatto quadrature points for these points provide also very accurate integration over the interaction area. To avoid reflections of the outgoing wave functions from the finite boundary we employ the exterior complex scaling (ECS) described by McCurdy and Stroud [14] for both electronic and nuclear coordinates given by

$$r'(r) = \begin{cases} r, & r < r_0, \\ r_0 + (r - r_0)e^{i\theta_r}, & r \geq r_0, \end{cases} \quad (49)$$

$$R'(R) = \begin{cases} R, & R < R_0, \\ R_0 + (R - R_0)e^{i\theta_R}, & R \geq R_0. \end{cases} \quad (50)$$

We should emphasize that the choice of r_0 and R_0 , where complex scaling starts must respect the following condition. Both the initial and test wave functions must be negligible beyond the boundary of the real region. This condition is sufficient in our implementation since we place all initial and test functions into the asymptotic regions where the interaction potential energy is already negligible or constant.

Perhaps the most important benefit of the FEM-DVR method with ECS is that the Hamiltonian is represented by a very sparse matrix. To take advantage of this sparsity we approximate the evolution operator (23) using the generalized Crank-Nicolson method [15], i.e., by the Padé approximant expressed as a product of simple rational terms which are applied subsequently to the wave function,

$$\psi(t + \Delta t) = e^{-iH\Delta t} \psi(t) \approx \prod_{j=1}^N \frac{(1 + c_j H \Delta t)}{(1 - c_j^* H \Delta t)} \psi(t), \quad (51)$$

where c_j denotes the j th root of the Padé approximant, N is the order of the approximation, and Δt the evolution time step. Using a sufficiently small time step ($\Delta t \rightarrow dt$) and sufficiently high order of the Padé approximation leads to accurate results of the evolution [17]. Note that since we use the exterior complex scaling, the Hamiltonian representation is no longer a Hermitian matrix and the evolution operator is no longer unitary (the wave function is suppressed beyond the scaling border). The integration over time in (27), (34) and other equations is approximated by the Simpson rule. Since the infinite integration over time is approximated by a finite integration we may expect inaccuracies for energies very close to zero.

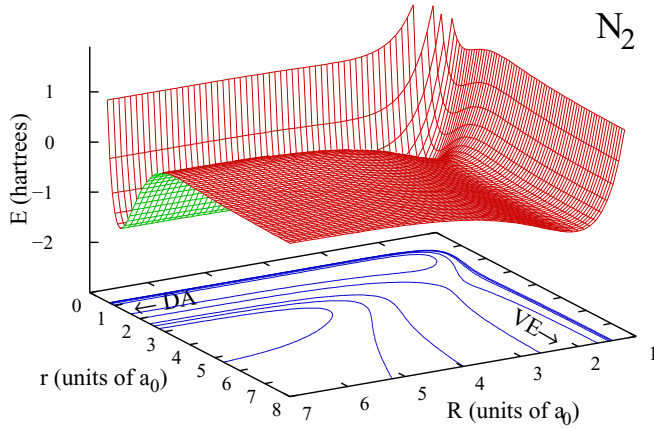


FIG. 1. The full 2D potential energy surface of the N_2 -like model shown at short distances.

VII. RESULTS

In this section we give an overview of the results for three models introduced in the papers [1] and [2]. We focus on describing the evolution of the two-dimensional wave functions and their comparison with the time-dependent LCP approximation and the comparison of the cross sections with the time-independent results. Probably the best way how to observe the time evolution of any system is to use animations. For the 2D models studied in this paper such animations are provided as Supplemental Material [18].

The interpretation of the cross section structures follows in Sec. VIII. The details of the numerical computations, such as the space discretization or the order of the Padé approximation to the evolution operator, may be found in the Appendix. For all three models we confine the investigated energy range to $[0, 0.2]$ a.u. in which resonant processes we are interested in take place.

A. N_2 -like model

The first model we will discuss is the N_2 -like model. The shape of the 2D model potential in the interaction region is shown in Fig. 1 and the potential energy curves of the LCP approximation obtained from the fixed-nuclei calculations for this model are shown in Fig. 2.

We start the evolution of the 2D model at time $t = 0$ with an incoming wave packet in the VE channel $v_i = 0$ given by (20) placed at $r_0 = 45$ with $\sigma = 6.0$ and $p_0 = -0.35$. Note that the mean impulse corresponds to kinetic energy of the electron $p_0^2/2 \simeq 0.06$. The width of the Gaussian wave packet is chosen in such a way that the Fourier-Bessel transform (22) covers the whole investigated range but quickly becomes negligible beyond. The order of the Padé approximant was set to $N = 3$ and the evolution time step to $dt = 1.0$. Note that the order of the Padé approximant could be chosen higher with a larger evolution time step and still provide accurate results of the evolution [17] but since the time step is also used for sampling the integration over time in the S -matrix elements its increment would decrease the accuracy of these computations.

We present a few snapshots of the evolved two-dimensional wave function in Fig. 3. At the beginning of the evolution

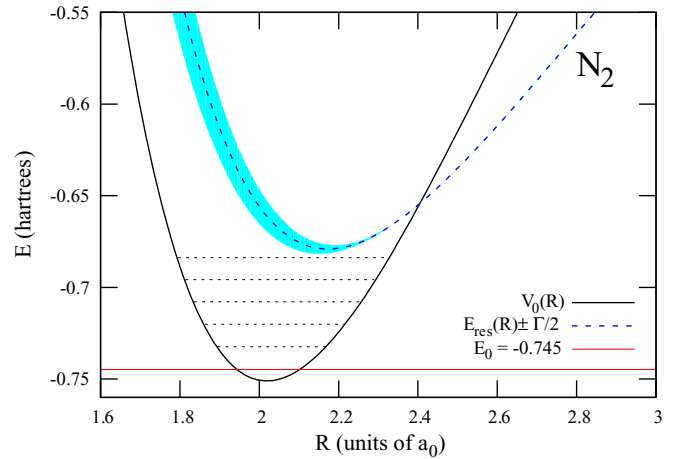


FIG. 2. The potential energy curves of the LCP approximation for the N_2 -like model. The solid black line shows the neutral molecule potential $V_0(R)$; the dashed blue line marks the resonant energy curve $E_{\text{res}}(R)$. The shaded area around the resonant energy curve shows the resonance width $\Gamma(R)$. The solid red line marks the neutral molecule ground state energy level; the dashed black lines represent several vibrationally excited states.

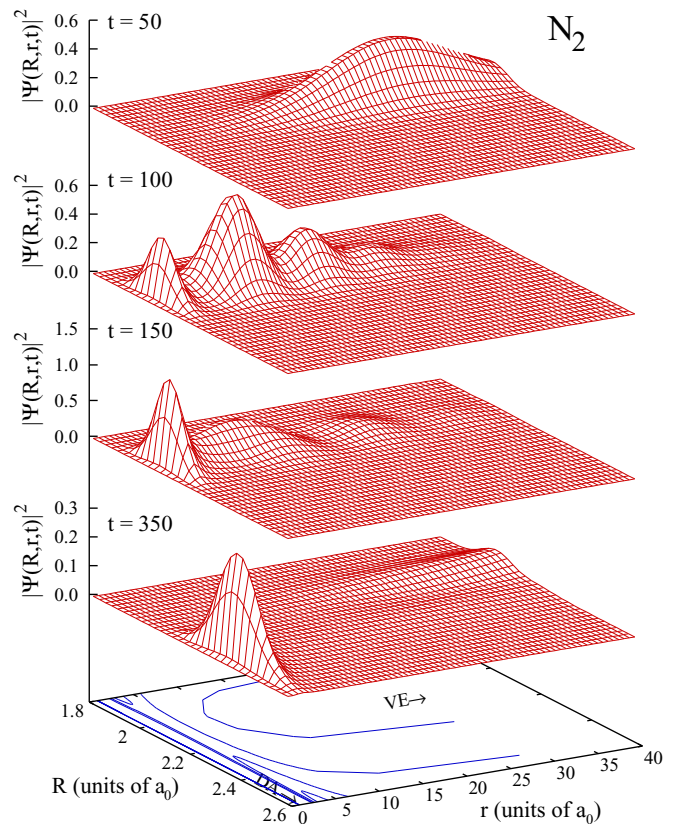


FIG. 3. Snapshots of the evolved wave function for the N_2 -like model. The evolution time is marked in the left corners. From the top we show the incoming wave packet ($t = 50$), the initial reflection to the VE channel ($t = 100$), the wave packet trapped behind the potential barrier ($t = 150$), and its motion towards larger internuclear distances ($t = 300$).

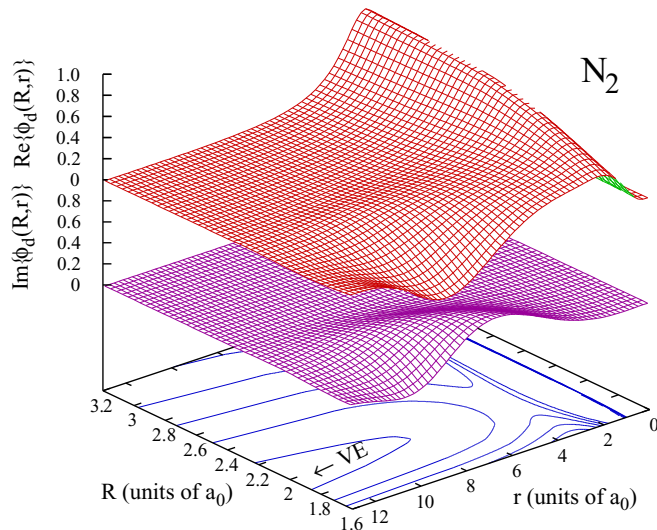


FIG. 4. The real (red) and imaginary (purple) part of the wave function of the physical choice of the discrete state $\phi_d(R,r)$ for the N_2 -like model. Note that orientation of the axes here differs from Fig. 1 for better visibility.

the initial wave packet moves towards the interaction region where a part of it tunnels through the potential barrier at $r \sim 2-5$ and is trapped in the well while the remaining part is reflected back and moves to the VE channels. At sufficiently large distances it is absorbed by the complex scaled part of the electronic coordinate to prevent reflections back to the interaction region. The trapped part of the wave packet moves slowly towards larger internuclear distances. Once it reaches distances $R \sim 2.2-2.6$ it is repelled back due to the increasing potential energy. At $t \sim 420$ the wave packet reaches the maximal value of the internuclear distance around $R \sim 2.4$. Since the dissociative channel is not accessible for the given energy range the whole wave packet is reflected back towards the interaction region. This motion is often referred to as the *boomerang motion*. In the interaction region a part of the wave packet penetrates back to the VE channels and leaves the interaction region. A small part of the wave packet remains behind the barrier and repeats the motion in the nuclear coordinate.

To compare the evolution of the two-dimensional wave function with the evolution of the wave function from the LCP approximation we project the 2D wave function to the physical choice of the discrete state for each internuclear distance. The real and imaginary parts of the discrete state are shown in Fig. 4. Note that the imaginary part is nonzero only for internuclear distances smaller than R_c , i.e., in the region where the energy of the fixed-nuclei electronic state $E_{\text{res}}(R)$ is above the neutral molecule potential energy $V_0(R)$. In Fig. 5 we present the comparison of the time evolution of these projections with the LCP approximation wave function. Note that the figure provides only information about relative changes in time since the LCP wave packet was rescaled and synchronized to the projections (see Sec. VIII for details). The significant differences occur at the beginning of the evolution, since the process of the trapping in the potential well is not included in the LCP approximation for it describes only

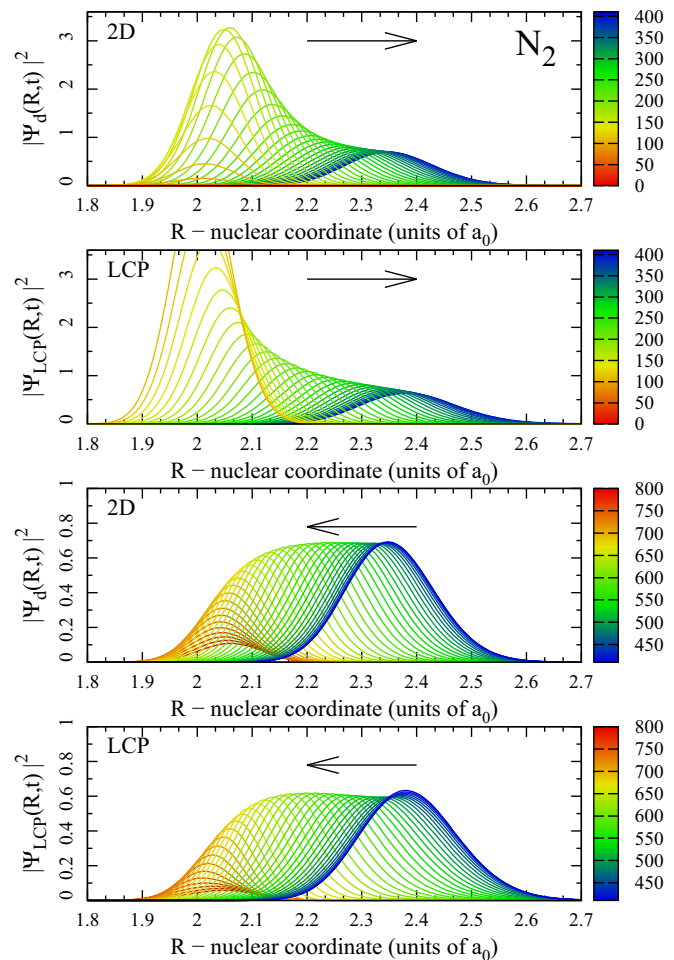


FIG. 5. Comparison of the time evolution of the 2D wave function projected onto the discrete state with the LCP wave function for the N_2 -like model. The time is marked by the color of the curve as indicated in the box on the right side of the panels. The incident wave packets were synchronized by $\Delta t \doteq 101$. The LCP wave packet was rescaled to match the projection normalization at $t = 419$, i.e., multiplied by factor 328 (see Fig. 20 and Sec. VIII for explanation).

the evolution of the trapped wave packet. The shapes of the functions are very similar otherwise.

We have set the cutoff time to $t_c = 4000$ a.u. $\simeq 100$ fs since the wave function amplitude in the interaction region becomes negligible. As mentioned before we have tested three methods for evaluation of the S -matrix elements. The test functions for the Tannor and Weeks approach have to be placed far enough, not only from the interaction region but also from the initial state so their overlap is negligible. We have set the positions to $r_0 = 75$ with the mean impulse $p_0 = 0.39$ and the width $\sigma = 6.0$. The position of the δ functions in the modified Tannor and Weeks approach and of the surface flux integration were both set to $r_0 = 75$ as well.

The resulting cross sections for three selected VE transitions are shown in Fig. 6 along with the time-independent calculation and LCP approximation results. The time-dependent calculation is in very good accordance to the reference time-independent result for all three studied methods. Note that the results are converged even at channel thresholds where

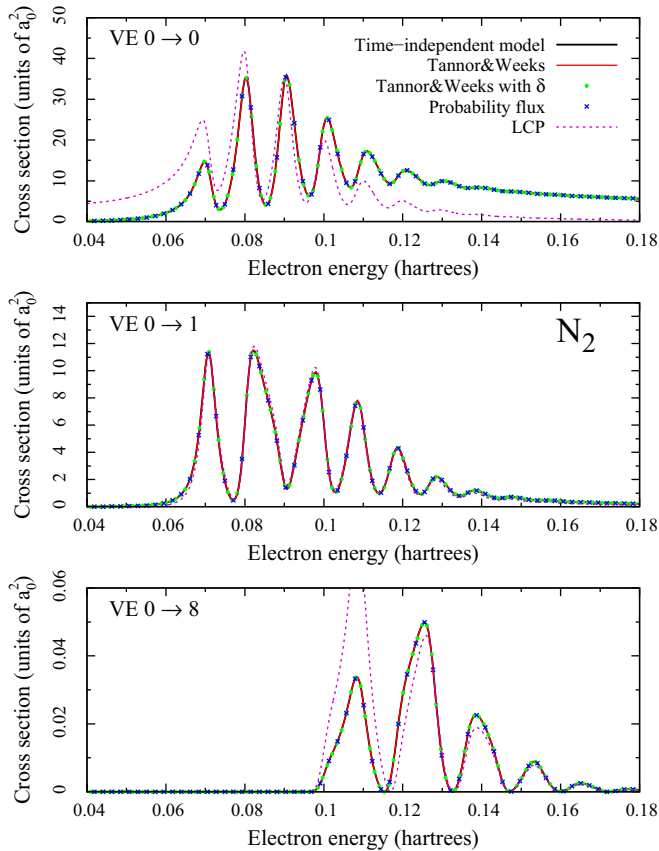


FIG. 6. The cross sections of the elastic and inelastic processes for the N_2 -like model at the cutoff time obtained by three methods of the S -matrix evaluation and by the LCP approximation are compared with the time-independent approach of the 2D model.

the energy of outgoing electron is close to zero (for example the $VE\ 0 \rightarrow 8$ cross section in Fig. 6 at the threshold energy $E \simeq 0.096$ goes to zero). The only noticeable inaccuracy of the time-dependent approach appears in the elastic scattering process for very low energies (not shown in Fig. 6). This inaccuracy results from Eqs. (38) and (39) when evaluated numerically close to zero energy.

To complete the discussion of results for N_2 -like model we show in Fig. 7 a comparison of the VE cross section for transition $0 \rightarrow 1$ calculated using the time-dependent approach presented in this paper with the result of Shandilya *et al.* [5] and with the experimental cross section of Allan [22] multiplied by a factor to have the same maximal value of the highest peak as our results. Although the 2D model was not meant for direct comparison with experiment one can see that the 2D N_2 -like model reproduces the basic features of the cross section rather well. Lower frequency of the oscillations at higher energies is due to a slightly incorrect shape of the potential energy curve of the molecular anion N_2^- to which the model parameters were fitted. On the other hand, the cross section of Shandilya *et al.* differs quite significantly from our and experimental result although it should be the same as ours because the model is the same. We should also note here that although it is not explicitly written in the paper by Shandilya *et al.* we suspect that Shandilya *et al.* also normalized their

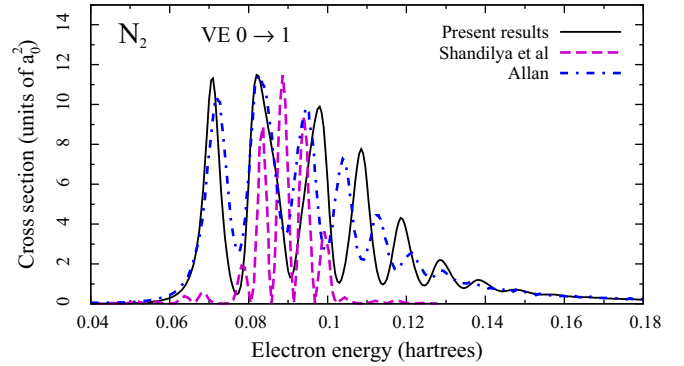


FIG. 7. Comparison of the $VE\ 0 \rightarrow 1$ cross section for the N_2 -like model with the result of Shandilya *et al.* [5] and with the experimental result of Allan [21].

theoretical cross sections (for each VE transition *separately* to get the same maximal value of the highest peak as in [1]) because their cross sections for all VE transitions have always the same maximal value as results in [1], which in our opinion makes further comparison of our results with their cross sections useless.

B. NO-like model

The second investigated case is the NO-like model. As in the previous case we show the image of the potential in the interaction zone in Fig. 8 and the derived potentials $V_0(R)$ and $V_{\text{res}}(R)$ in Fig. 9. Note that the minimum of $V_{\text{res}}(R)$ is now behind the crossing point of the potential curves forming an *outer well* (outside the autodetachment region). Therefore longer living states in this outer well can be expected to form during the dynamics. Also note that since in this model the DA channel is open for energies $E \gtrsim 0.175$, we have to extend the discretization in the internuclear coordinate; details may be found in the Appendix.

As in the previous case we start the evolution with the initial state in the VE channel $v_i = 0$ with the initial position of the Gaussian wave packet placed at $r_0 = 45$, with the mean impulse $p_0 = -0.35$ and the width $\sigma = 6.0$. The order of the

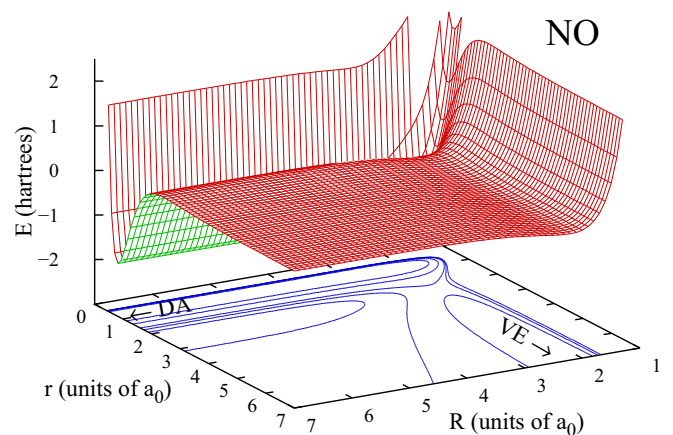


FIG. 8. The full 2D potential energy surface of the NO-like model shown at short distances.

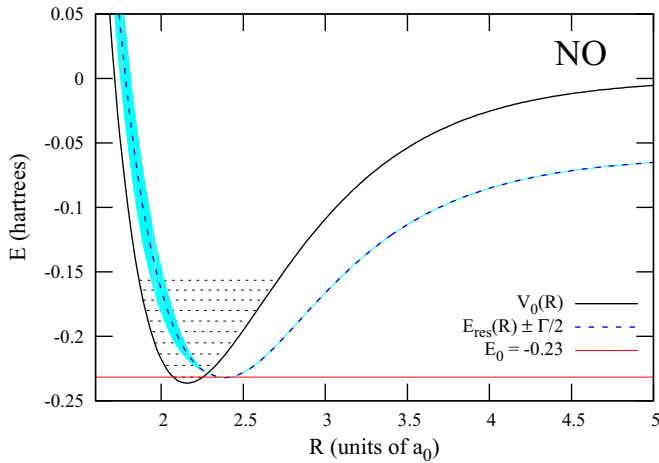


FIG. 9. The potential energy curves $V_0(R)$ (solid black line) and $E_{\text{res}}(R)$ (dashed blue line) with the resonance width $\Gamma(R)$ marked as the shaded area around $E_{\text{res}}(R)$ for the NO-like model.

Padé approximation was set to $N = 3$ and the evolution time step to $dt = 1$. The beginning of the evolution is practically the same as in the previous case. The initial wave packet reaches the interaction region where it hits the potential barrier. A part of the wave packet penetrates to the potential well and the other part is reflected to the VE channels, leaves the interaction region and being consumed by the imaginary part of the complex scaled electronic coordinate it quickly vanishes.

Meanwhile the trapped wave packet starts to move in the internuclear coordinate. We present images of the evolved wave function in Fig. 10. The noticeable difference from the N_2 -like model appears at the end of the boomerang motion when the returning wave packet penetrates back to the VE channels. The wave packet has no longer one smooth peak in the internuclear coordinate. The second peak appears at $R \sim 2.4$ where the minimum of the potential energy curve $E_{\text{res}}(R)$ is; see Fig. 9.

That the dynamics of this model slightly differs from the N_2 -like model is nicely visible from the projections onto the discrete state. This state is very similar to the discrete state used in the N_2 -like case, with only small differences in the interaction region where it changes slightly more rapidly with the decreasing internuclear distance. Since it is so similar we omit the figure. The evolution of the projections along with the LCP approximation wave function may be found in Fig. 11. The top panel shows the process of initial electron capture into the resonant state and the motion of the captured part of the wave packet towards larger internuclear distances. The capture is again naturally missing in the LCP approximation. The LCP wave function was rescaled and synchronized to match the projection at the maximal internuclear distance (see again Sec. VIII for details). Note that the maximal mean internuclear distance is slightly different for the projection ($R_{\text{max}} \simeq 2.75$) and for the LCP approximation ($R_{\text{max}} \simeq 2.7$). However, this maximal distance for projections is strongly dependent on the parameters of the initial wave packet (the higher the mean energy of the wave packet the larger R_{max}). The second pair of panels shows the motion back to the interaction region and the process of decaying of the resonant state.

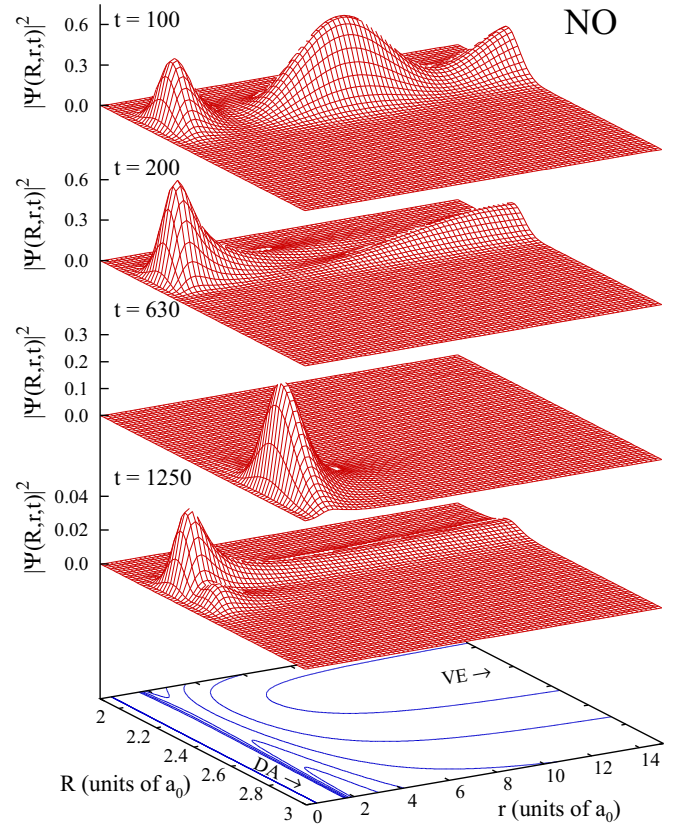


FIG. 10. Snapshots of the evolved wave function for the NO-like model. The upper image ($t = 100$) shows the initial reflection of the incident wave packet and the second one ($t = 200$) capturing of a part of the wave function behind the potential barrier. Note that it is localized in slightly smaller internuclear distance than the incident wave function corresponding to the fact that the probability of capturing is significantly higher for smaller internuclear distances. The third snapshot ($t = 630$) shows the trapped wave packet at the maximum of the boomerang motion and the last one ($t = 1250$) the penetration of the wave packet back to the VE channels.

Another significant difference between models is visible in the region around $R \approx 2.4$, magnified in the third pair of panels, which points to the failure of the LCP approximation. As the evolution continues the two-dimensional wave function decays more slowly suggesting the presence of a long-living state. The cutoff time was set to $t_c = 35\,000$ since the normalization of the two-dimensional wave function dropped enough below 10^{-9} . We present the cross sections for a few VE channels and the DA channel obtained by all three methods described above compared to the time-independent calculation and LCP approximation in Fig. 12. Again the results agree with the time-independent ones for almost all investigated energies. Small distortions appear at the very low energies, as should be expected since the time-dependent calculation would need much longer time to provide accurate results, and also in the DA cross section which is very small and all numerical inaccuracies are enhanced.

Surprisingly, some of the very low energy inaccuracies may also originate from too large evolution time step dt if the Fourier-Bessel coefficients decay too slowly with increasing

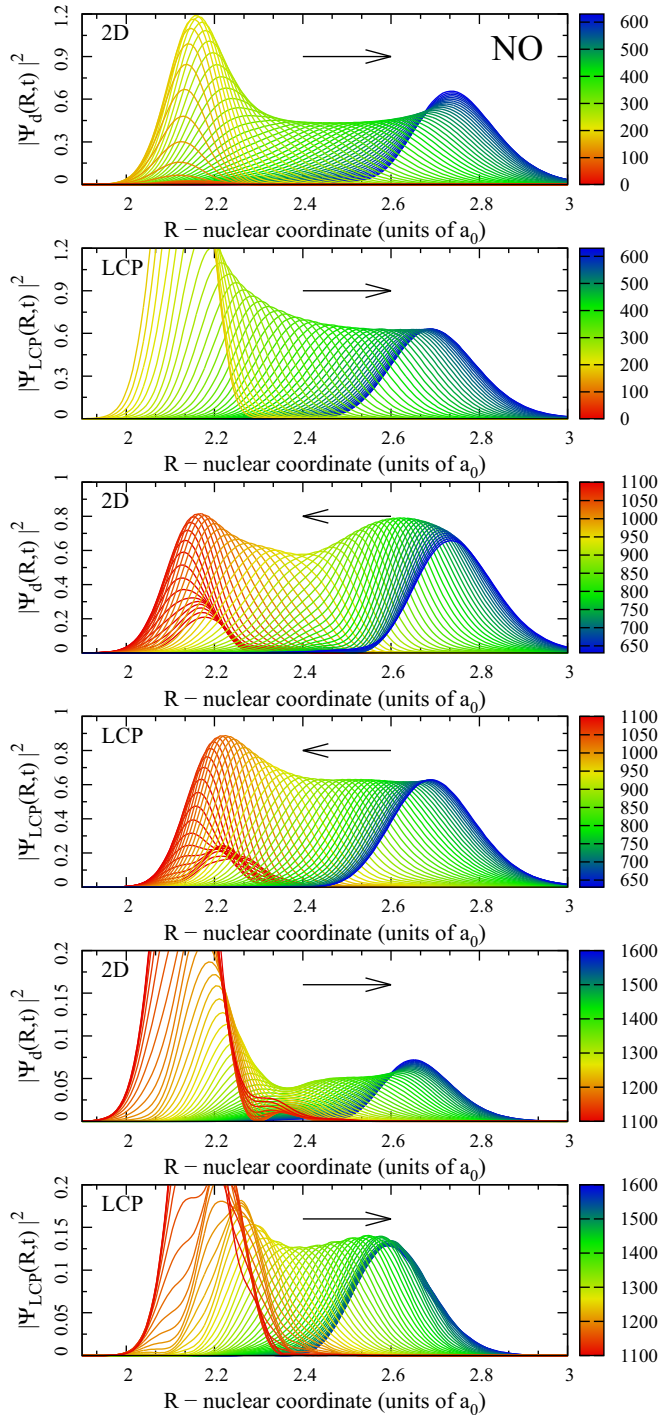


FIG. 11. Comparison of the time evolution of the 2D wave function projected onto the discrete state with the LCP wave function for the NO-like model. The LCP wave packet was synchronized with the projection by $\Delta t = 176$. For better comparison we have rescaled the LCP wave packet to the projection in time $t = 637$ by factor 287 (see Fig. 22 and Sec. VIII for explanation).

energy. The very low energy contributions may be distorted by contributions of high energies for which $E_1 dt \approx E_0 dt + 2\pi$, where E_0 is some energy from the investigated range. This effect can be either suppressed by a different choice of the initial wave packet energy distribution or by decreasing the time step.

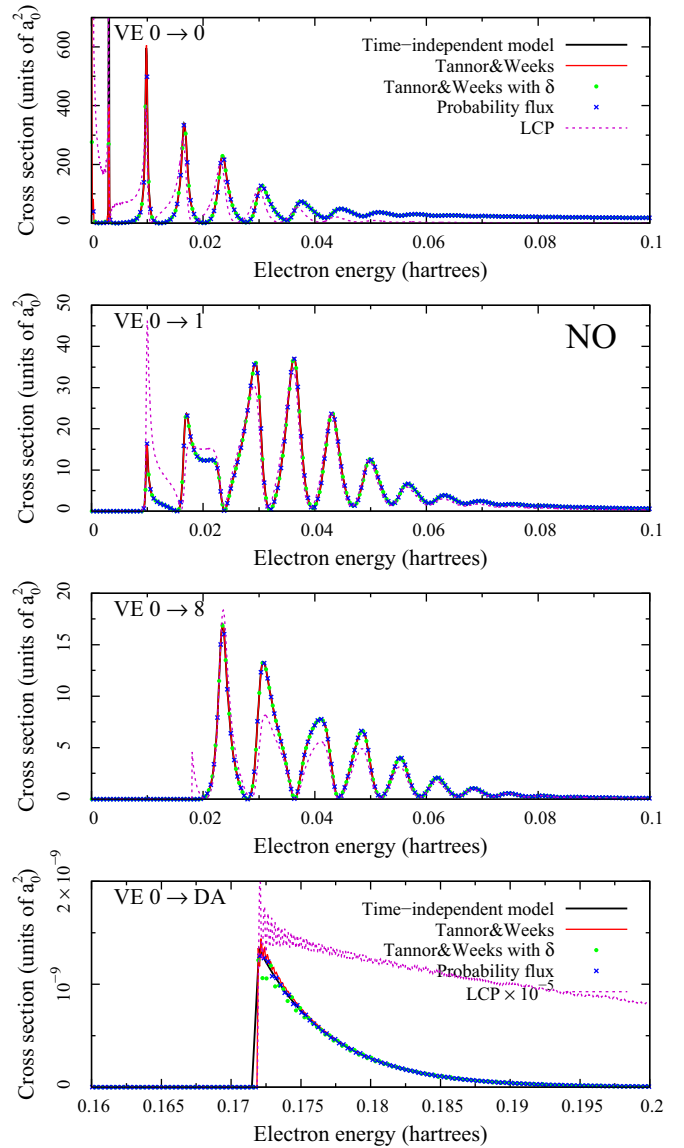


FIG. 12. The cross sections of the elastic process, vibrational excitation $0 \rightarrow 1$ and $0 \rightarrow 8$, and the dissociative attachment for the NO-like model at the cutoff time $t_c = 35000$ obtained by three methods of the S -matrix evaluation along with the LCP approximation results compared to the time-independent approach of the 2D model.

Even though the values of the DA cross sections are very small the results agree well with the time-independent ones for all three methods. The results could be even further improved by a better choice of the initial parameters, but since we did not expect to get any new information from such large computations we have not pursued the goal any further. We should also note that the DA cross sections were obtained separately from the VE cross sections since the grid parameters and time step were chosen differently resulting in lower computational requirements and less computational time.

C. F_2 -like model

The F_2 -like model significantly differs from the previous two models. As one may see from Fig. 13 the full 2D potential

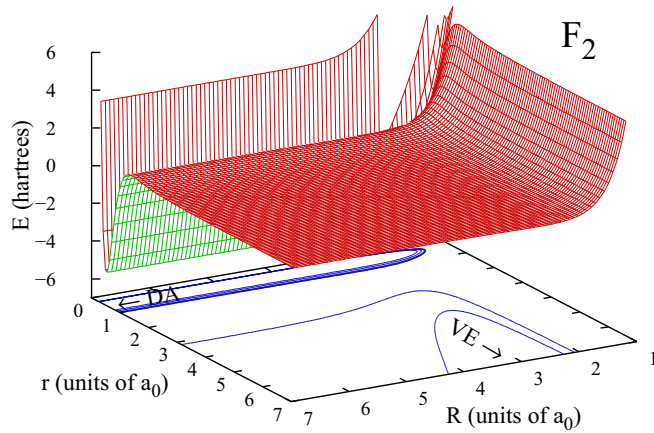


FIG. 13. The full 2D potential energy surface of the F_2 -like model shown at short distances.

forms a deep but very narrow well close to the origin of the electronic coordinate; therefore the electronic grid was refined mainly in the region $[0, 1]$. As one can see from the LCP approximation potentials in Fig. 14 the DA channel is accessible for all energies and the negative molecular ion potential $E_{\text{res}}(R)$ crosses the neutral molecule potential $V_0(R)$ very steeply resulting also in significant increase of nuclear coordinate grid density (see the Appendix for details).

The parameters of the initial wave packet and time evolution were set to the same values as in the NO-like model. We present a few snapshots from the evolution of the wave packet for this model in Fig. 15. After the wave packet hits the interaction region, a part of it is reflected by the potential barrier; another part penetrates through and becomes trapped creating a smooth peak close to $r \sim 0.5$ and $R \sim 2.6$. After around 50 units of evolution time a distortion of the trapped wave packet appears. Since the trapped part of the wave packet is located in the region of a steep potential slope in the nuclear coordinate, it is quickly accelerated towards larger internuclear distances. At the same time the part of the wave function which is reflected to the VE channels is slowly withdrawing. Since the complex

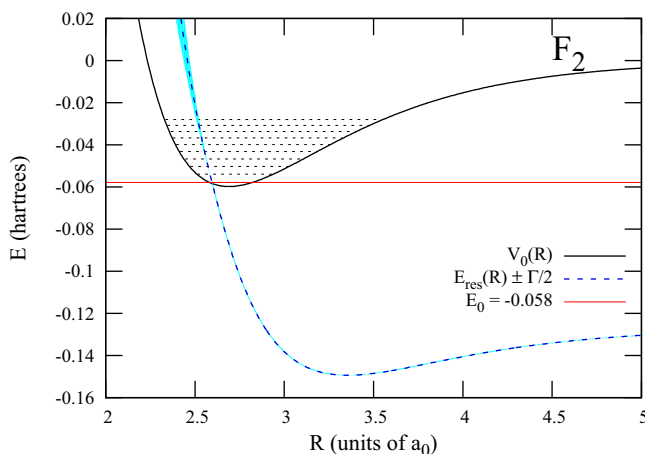


FIG. 14. The potential energy curves $V_0(R)$ (solid black line) and $E_{\text{res}}(R)$ (dashed blue line) with the resonance width $\Gamma(R)$ marked as the shaded area around $E_{\text{res}}(R)$ for the F_2 -like model.

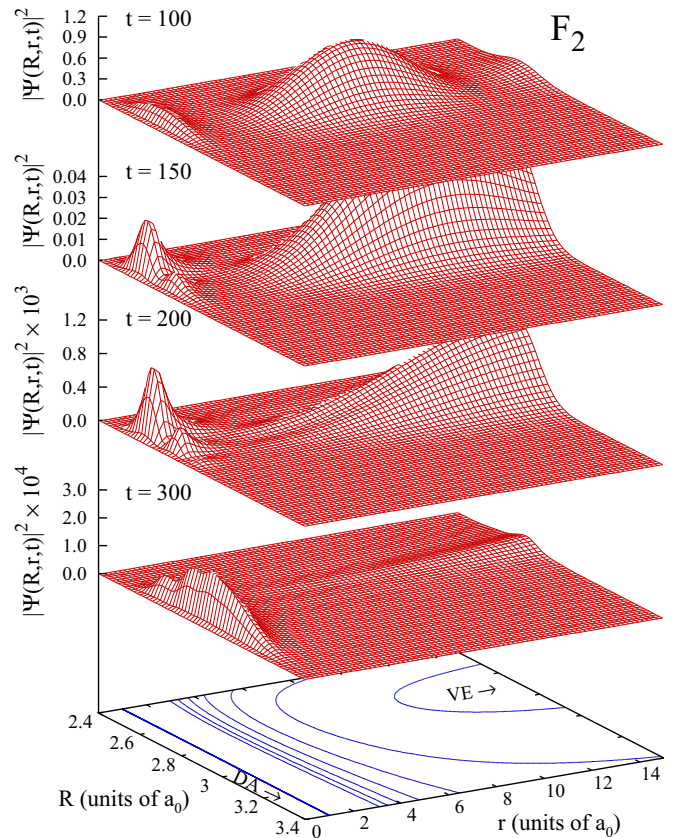


FIG. 15. Snapshots of the evolved wave function for the F_2 -like model. The beginning of the evolution is similar to the NO case but there is no reflection of the trapped wave packet at larger internuclear distances. The evolution time is marked in the left corners; the scaling of the figures is marked on the z axis.

phase of the outgoing waves to the VE channels changes slowly with the nuclear coordinate and the complex phase of the waves outgoing to the DA channel changes quickly, their presence in the same region results in an interference. Once the trapped wave packet moves to larger internuclear distances the interference is no longer visible. Since there is no potential barrier in the direction of increasing internuclear distance, the wave packet cannot be reflected back and therefore it moves further to the DA channel resulting in dissociation of the molecule.

To compare the full dynamics with the LCP approximation, we again projected the 2D wave function on the discrete state, which is shown in Fig. 16. It is clear that this state changes rapidly with decreasing internuclear distance once the potential $V_{\text{res}}(R)$ crosses the neutral molecule potential $V_0(R)$.

The interference described above in the 2D dynamics is also clearly visible in the evolution of the projection onto the discrete state in Fig. 17 where its comparison with the LCP wave function is shown. Note that there is no interference in the LCP approximation, which is natural since the interaction with the electronic continuum is approximated by a simple imaginary part of the local potential $V_{\text{res}}(R)$. As the evolution continues and the interference in the projections disappears, the wave packets seem to be similar although the projection is

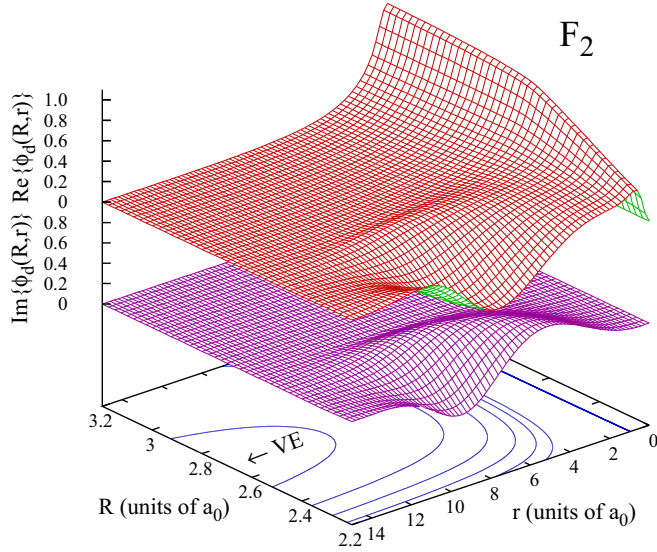


FIG. 16. The real (red) and imaginary (purple) part of the wave function amplitude of the discrete state $\phi_d(R, r)$ for the F_2 -like model.

much wider than the LCP wave function. Since the width of the trapped wave packet is strongly dependent on the initial 2D wave packet, there is no physical significance in this difference.

Since the motion is aperiodic the cutoff time $t_c = 15\,000$ was chosen simply to be large enough for the outgoing waves to leave the real region of the grid. The cross sections in Fig. 18 show again a good accordance of the time-dependent results with the time-independent ones for almost all energies. Only for very low energies the elastic and DA cross sections are slightly distorted. These inaccuracies are due to the initial setup of parameters and finite integration time and could be further improved with cost of the computational resources.

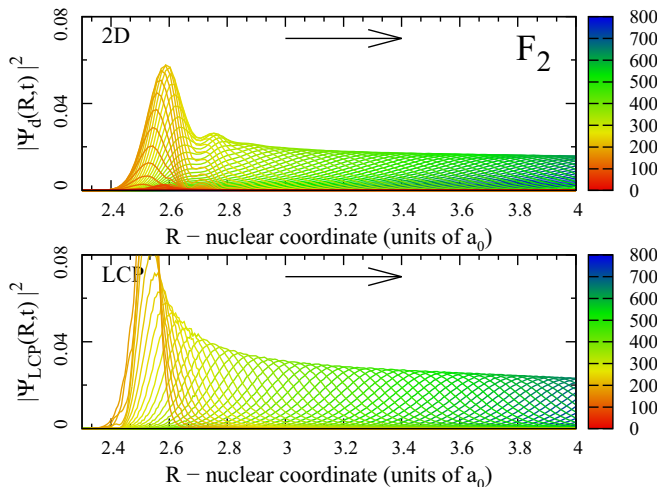


FIG. 17. Comparison of the 2D wave function projection onto the discrete state with the LCP wave function for the F_2 -like model. The LCP wave packet was synchronized with the projection to match in the beginning of the outgoing motion by $\Delta t = 177$. The LCP wave packet was rescaled for better comparison. The evolution time is marked by the color of the curve corresponding to the color bar on the right side of the panels.

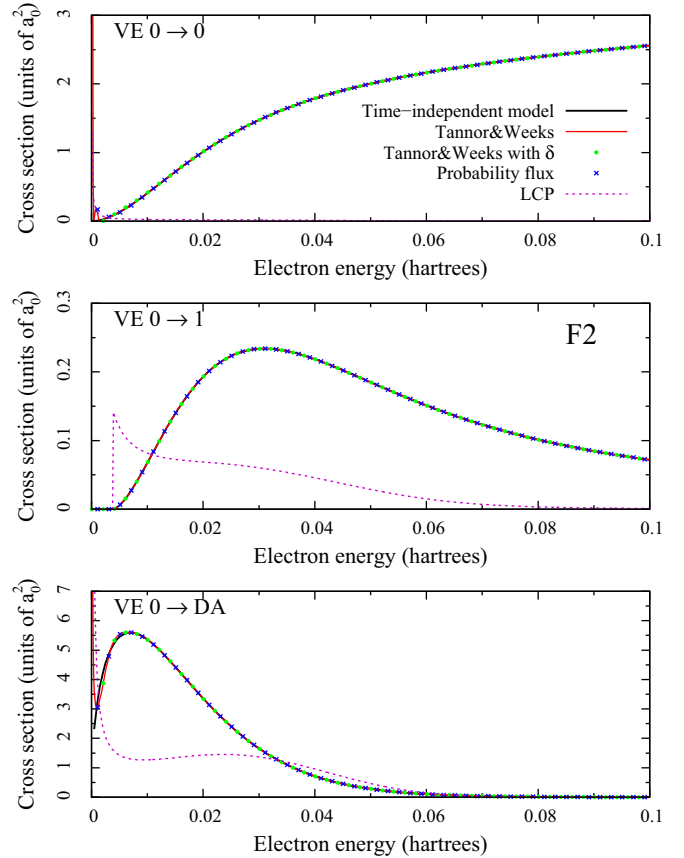


FIG. 18. The elastic, $VE\ 0 \rightarrow 1$ and DA cross sections for the F_2 -like model at the cutoff time $t_c = 15\,000$ obtained by three approaches to the S -matrix evaluation.

Again, since we did not expect any new information to be obtained we have not pursued this goal any further.

The comparison of the 2D model cross sections with the LCP approximation results was already deeply investigated in [2] and therefore we leave the topic with a simple comment that the interference during the evolution of the 2D wave function manifests the nontrivial nature of the motion; i.e., it is a direct result of breaking the Born-Oppenheimer approximation. It also reveals the inability of the LCP approximation to describe such systems where the process of the penetration through the barrier and initial repulsion is not sufficiently separated in time, i.e., where there is a non-negligible overlap between the outgoing waves to the VE channels and DA channel already in motion.

VIII. INTERPRETATION OF THE CROSS SECTIONS

The actual vibrational excitation cross sections of resonant collisions of electrons with diatomic molecules N_2 [19–22] and NO [23,24] are very similar to ones obtained using the N_2 -like and NO -like models shown in Figs. 6 and 12. The oscillatory structures appearing in the VE cross sections are often explained as an interference of the fast direct decay of the electronic resonant state of the negative molecular ion in the autodetachment region (to the left from the crossing point of the potential energy curves of the neutral molecule and

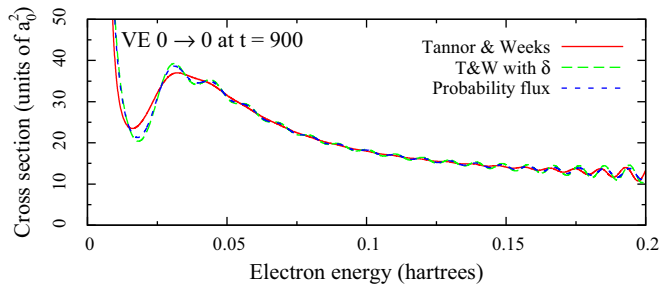


FIG. 19. Comparison of the elastic scattering cross sections obtained by three investigated methods at time $t = 900$ for the NO-like model.

the anion; see Figs. 2 and 9) with the time-delayed decay of this state due to vibrational motion out of the autodetachment region and back. This mechanism is usually referred to as the *boomerang* model [8,9] which is a valid explanation of oscillatory structures in the VE cross sections for certain systems (for example for H_2 molecule [25]), but it does not explain the origin of irregularities in these structures. Most of the calculations on real systems are actually performed within the time-independent framework in which the explanation of the structures and especially of appearance of the asymmetric peaks is much more complicated (see, e.g., [10]).

Here we take an advantage of the time-dependent formulation of the two-dimensional model to study in detail the origin of the oscillatory structures including the asymmetric peaks appearing in the VE cross sections in Figs. 6 and 12. We will demonstrate that the simple boomerang mechanism provides an explanation only to a regular oscillatory structure but to explain asymmetry of peaks one has to consider further vibrational motion of the negative molecular ion and even long-lived states in the potential well outside the autodetachment region.

Before we proceed with the interpretation of the cross sections we discuss the comparison of the approaches to the S -matrix computation. Up to this point we have treated all three investigated methods equally since the results at the cutoff time were practically the same. The key difference arises once we try to compare the results at early times. As an example we show the elastic cross section evaluated at $t = 900$ for the NO-like model in Fig. 19. Note that this time there is a significant difference between the three methods. Both the Tannor and Weeks method with the δ function and the probability flux approach oscillate while the original method of Tannor and Weeks oscillates only at higher energies. It is even possible to further improve the results of the Tannor and Weeks method by modifying the parameters of the test functions or of the initial state. We conclude that the time-energy Fourier transform in the Tannor and Weeks method is much smoother. Therefore it is more suitable for the early cutoff time computations and in this section we will show results only for this method.

A. N_2 -like model

We start with results for the N_2 -like model. In Fig. 20 we show the evolution of the mean internuclear distance and the

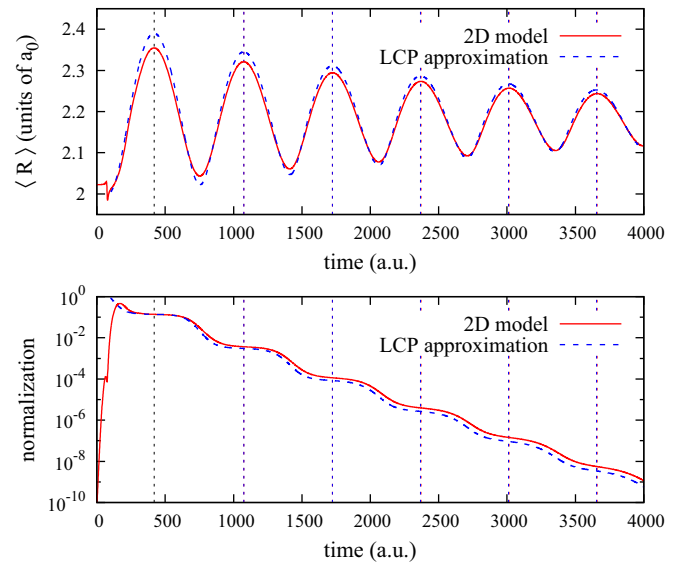


FIG. 20. The mean internuclear distance of the projections and the LCP wave packet (top panel) and their normalization (bottom panel) as functions of the evolution time. The vertical dashed lines mark the positions of the maxima of the mean internuclear distance. The position of the first maximum at $t = 419$ was used to synchronize the evolution within the LCP approximation by $\Delta t = 101$ and also to adjust normalization of the LCP wave packet for better comparison.

normalization of both the projections onto the discrete state and the LCP approximation wave packet. We have used the position of the maximal value of the mean internuclear distance (marked by vertical dashed lines) to synchronize the motion of the projections with the LCP wave packet and we rescaled the normalization of the LCP wave packet for better comparison. It is clear that the motion in the nuclear coordinate resembles the motion of a damped harmonic oscillator. From the distance between two maxima of the mean internuclear distance we were able to determine the period of the nuclear motion to $T \approx 655$ a.u. ≈ 16 fs. The normalization curves (bottom panel of Fig. 20) shows decrement only in the moments of minimal mean internuclear distance. This behavior corresponds to the fact that the wave packet can tunnel through the potential barrier back to the VE channels only in the autodetachment region close to the minimum of the neutral molecule potential $V_0(R)$, in this case at $R \sim 2$. Since at the time around $t \sim 400$ – 500 the wave packet is at its maximum mean internuclear distance around 2.4 and the normalization is almost constant, forming a wide plateau, we may assume the contribution to the cross sections from the passed evolution to be well separated from the subsequent contributions. The cross sections of the full 2D model evaluated at $t = 600$ are marked by dashed red lines and for LCP at $t = 400$ by blue dotted lines in Fig. 21. As we can see the initial reflection of the wave function produces one wide and smooth peak in all VE cross sections except unphysical peaks at threshold energies due to slower motion of corresponding outgoing waves. A similar shape appears in the LCP cross sections although it is slightly misplaced for the elastic scattering.

As the evolution continues another contribution from the so-called *boomerang* motion is added to the cross sections. Since

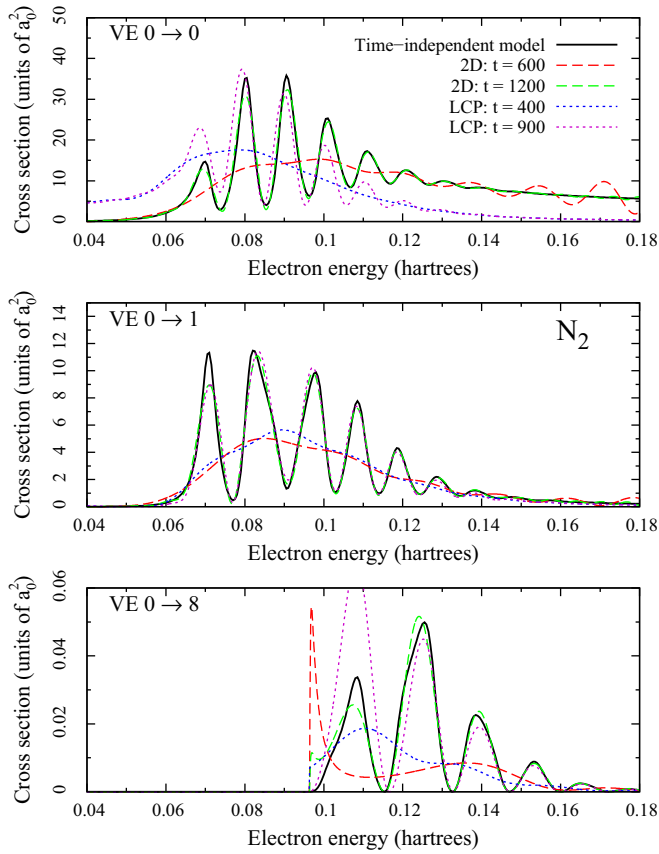


FIG. 21. The elastic and VE cross sections for two chosen transitions evaluated at significant values of the evolution time. The dashed lines stand for the 2D model, the dotted lines for the LCP approximation. See also Supplemental Material [18] for videos of the cross sections as functions of time.

it is again well separated from the subsequent contributions we may take a look at the updated cross sections at the moment of the maximal mean internuclear distance at $t = 1200$ for the 2D model and at $t = 900$ for the LCP approximation. The results are shown in Fig. 21 by the green dashed and pink dotted curve for the 2D and LCP models, respectively. This time a series of symmetrical peaks appears modulating the previously obtained shape. Note that the time-independent results are still slightly different from the ones obtained after the first vibrational period, mostly where the structures are asymmetrical. Apparently at least one more contribution (after another vibrational period) is needed to form the proper shape of the cross sections.

During the further evolution the normalization quickly decreases. As the normalization drops by 8 orders of magnitude around the time $t_c = 4000$ further contributions to the cross sections become negligible and there is no point in evolving the wave functions any further. Thus we set t_c as the cutoff time. The resulting cross sections were already discussed in Sec. VII.

B. NO-like model

Again we start with the comparison of mean internuclear distances and normalization for both the projection of the 2D

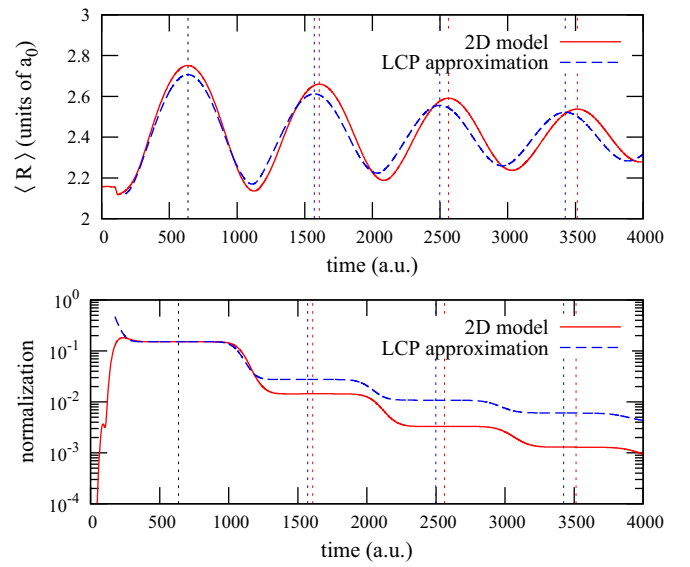


FIG. 22. The mean internuclear distance of the projections and LCP wave packet (top panel) and their normalization (bottom panel) as functions of the evolution time. Both mean internuclear distance and normalization curves were synchronized by the position of the first maximum of the mean internuclear distance at $t = 637$, with $\Delta t = 176$.

wave function onto the discrete state and the LCP wave packet, which are arranged in Figs. 22 and 23. Note that the motion in both models again resembles the damped harmonic oscillator. Also note that this time the frequency of the oscillations and the speed of the normalization decrement differ significantly for the 2D model and the LCP approximation which means that the nuclear dynamics for this system is not properly described by the LCP approximation and leads to a failure of the LCP approximation at lower energies (see Fig. 12). We have determined the period of the nuclear motion of the 2D wave packet to $T \approx 971$ a.u. ≈ 23 fs. The motion takes

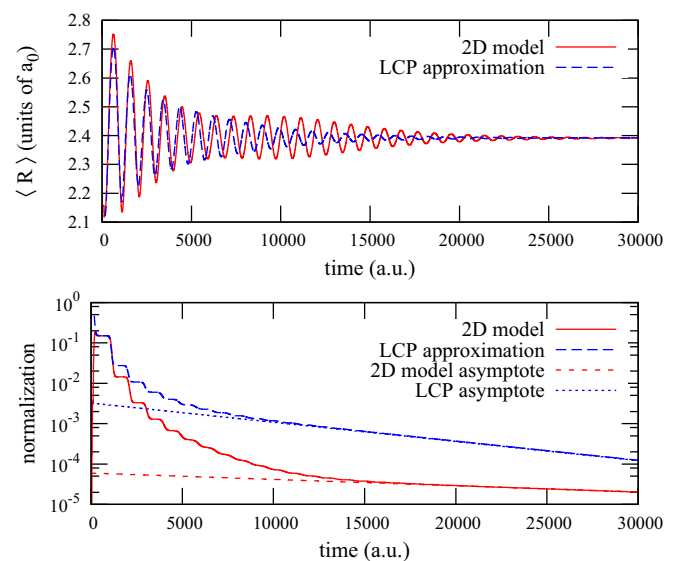


FIG. 23. The same as in Fig. 22 but for times up to 30 000 a.u.

place at distances from $R \sim 2.1$ to $R \sim 2.8$. The positions of the maximal mean internuclear distance again served as the separation points of the contributions to the cross sections. Decrease of the normalization in the NO-like model is much slower than in the N_2 case and thus many more contributions have to be included to obtain the converged cross sections. Another striking feature in Fig. 23 is a long, linear (in logarithmic scale) tail of both 2D and LCP curves. Such behavior points to an existence of a long-lived state which, as we will see, is responsible for a high, narrow peak in the elastic cross section.

For clarity of figures we omit results obtained within the LCP approximation in the following discussion. The interpretation of the structures within the LCP approximation would be very similar. As in the N_2 case the initial reflection contribution to the cross section at $t = 900$ produces a wide smooth peak in each VE channel shown as pink dotted curves in Fig. 24 where the elastic (upper panels) and VE $0 \rightarrow 1$ (lower panels) cross sections integrated up to particular times are presented. The results obtained for short times show pronounced threshold peaks due to slow motion of corresponding outgoing waves. These peaks later disappear as more contributions from slower outgoing waves are included.

At the time $t = 1800$ there are two contributions in the cross sections (blue dash-dotted curve): the initial reflection of the wave packet without nuclear motion is interfering with the wave packet leaving the autodetachment region after the boomerang motion. If there were no other contributions the resulting cross sections would consist of pure regular boomerang oscillations, but unlike in the N_2 case there are significant differences from the final (time-independent) cross sections; especially the peaks at lower energies in the elastic cross section are much narrower and higher and structures in the VE $0 \rightarrow 1$ cross section are very asymmetrical.

As the evolution continues and more contributions are integrated we can observe formation of these asymmetrical and narrow structures. Each narrow peak in the cross sections corresponds to a quasibound vibrational state of the molecular negative ion (states in the dashed blue potential in Fig. 9). The lower the energy of the state, the smaller its width, the larger its lifetime, and the narrower the corresponding structure. In the elastic cross section the maxima of boomerang oscillations ($t = 900$) are more or less at the same energies as the quasibound states and peaks are rather regular. On the other hand in the VE $0 \rightarrow 1$ cross section the maxima of boomerang oscillations are at different energies than these quasibound states which results in highly asymmetrical structures. Their forming in time can be observed in Fig. 24 from which we can estimate lifetimes of quasibound vibrational states. For example the first peak in the VE $0 \rightarrow 1$ cross section forms fully at $t > 10\,000$ and corresponds to the second vibrational state in the potential $V_{\text{res}}(R)$ of the NO-like model. The lowest lying state (the first peak in the elastic cross section) has a lifetime of more than 30 000. In Fig. 25 we show populations of quasibound vibrational states of the negative molecular ion [eigenstates in the potential energy $V_{\text{res}}(R)$] in the projection of the 2D wave function on the discrete state as a function of time which we computed as $|\langle v' | \Psi_d(t) \rangle|^2$. We show only results for the first four vibrational states for clarity; populations of higher states behave similarly to the population function for $v' = 3$

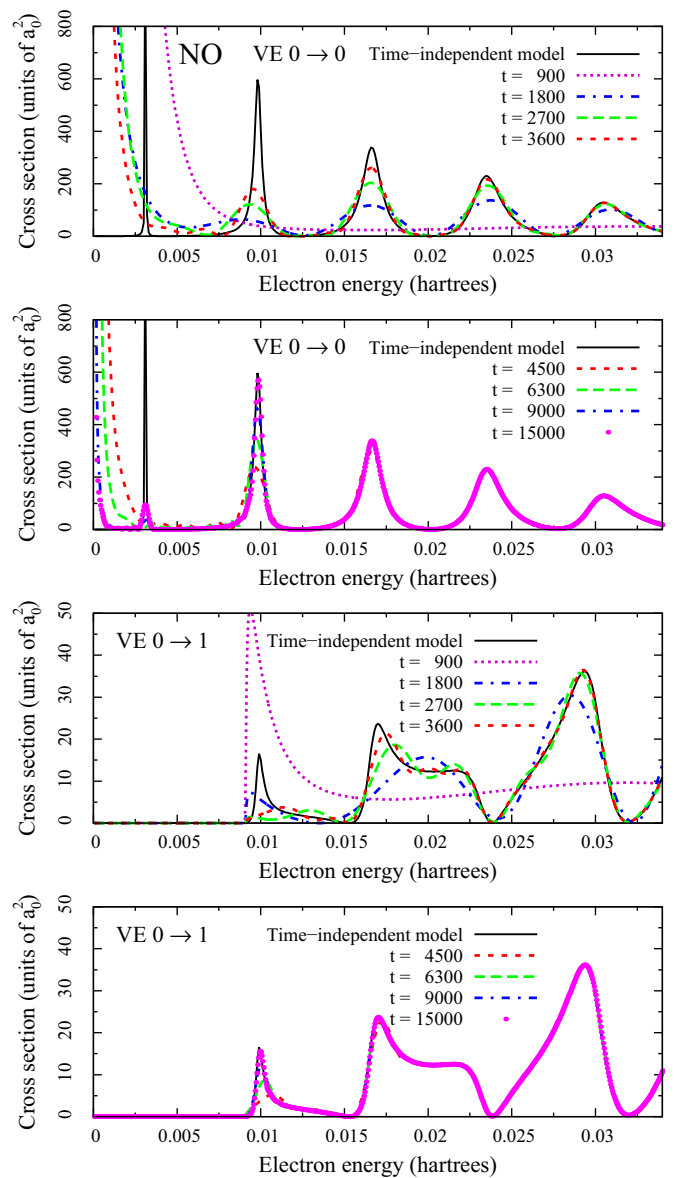


FIG. 24. The elastic and VE transition $0 \rightarrow 1$ cross sections at significant values of the evolution time. All results are for the full 2D NO-like model. See also Supplemental Material [18] for videos of the cross sections as functions of time.

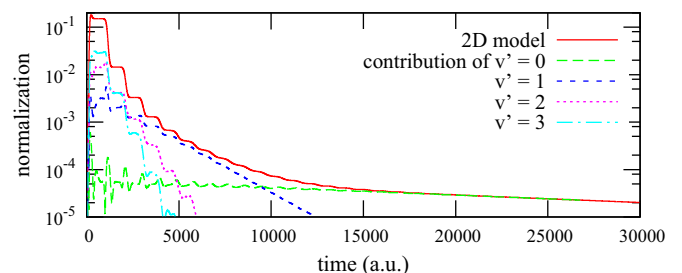


FIG. 25. The normalization of the projection of the 2D wave function on the discrete state for the NO-like model and contributions to this normalization of the first four quasibound vibrational states of the molecular negative ion as functions of the evolution time.

but decay even faster. We can observe in Fig. 25 that the higher lying vibrational states are more populated at the beginning but decay rapidly; on the other hand the low lying states survive for much longer time in accordance with the long formation time of peaks in the VE cross sections.

IX. CONCLUSION

In this work, we have investigated the two-dimensional model of the collisions of electrons with diatomic molecules within the time-dependent framework and solved the specific model problems numerically. To extract the S matrix from the time-dependent wave function we used three different methods and all results for energies of interest are in a perfect agreement with the cross sections obtained within the time-independent framework.

The results provided deep insight into the dynamics of the low-energy electron collisions with diatomic molecules and enabled us to find out the origin of all structures in the vibrational excitation cross sections, discussed in detail in Sec. VIII. For real systems one could perform similar time-dependent calculations within the local complex potential approximation or the nonlocal resonance model and thus interpret the results in the same way.

As we have shown, the vibrational excitation cross sections for diatomic molecules quite often result from several contributions separated in time and their shape is given by the interference between these contributions. More importantly the asymmetrical shapes in the cross sections are produced by more than two contributions; thus the terms *boomerang motion* and *boomerang oscillations* are not quite accurate. The terms *oscillatory motion* and *oscillatory structure* are in this context more appropriate.

ACKNOWLEDGMENTS

This work was supported by the Grant Agency of the Czech Republic (GACR No. 208/10/1281), by Charles University in Prague (GAUK No. 170910), and by the Ministry of Education, Youth, and Sports of the Czech Republic (SVV 260211).

APPENDIX: TIME EVOLUTION AND GRID PARAMETRIZATION

In this section we specify the parameters used to solve numerically the time evolution of the discussed two-dimensional model. All quantities are given in atomic units.

The electronic and nuclear coordinates were discretized by the finite-element method with the basis consisting of Lagrange interpolation polynomials constructed from Gauss-Lobatto quadrature points. The number of quadrature points n_q was the same in each element but differed for electronic and nuclear coordinates and for different models. The shape of the potentials shown in Figs. 1, 8, and 13 can be used for determining the parameters of coordinate discretization; e.g., it is necessary to use more elements for those areas, where the potential has deeper wells. Final parameters used in our calculations for three studied models are given in Table II. We should note that we had to increase the density of the discretization in the real region of the internuclear coordinate for the NO-like and F_2 -like models to be sufficiently dense for placing the DA channel test function.

To absorb the outgoing wave functions, the exterior complex scaling method was applied in both coordinates and the rotation angles θ used for a particular model can be also found in Table II. For the time evolution operator we used the diagonal Padé approximation (51) of order 3 which is sufficiently accurate with time step $dt = 1.0$ a.u. ≈ 0.024 fs for all three studied models.

TABLE II. The parametrization of FEM-DVR-ECS grids for both nuclear and electronic coordinates for all three investigated models, given in atomic units. All grids started at the origin of the coordinates and the number of elements under the specified distance is the number of elements on the interval from the previous distance to the specified one, not from the origin. Asterisks denote the exterior complex scaled regions.

N ₂ , electronic coordinate: $n_q = 10, \theta = 35.0$														
distance	5.0	7.0	10.0	90.0	100.0*	110.0*	210.0*							
elements	5	1	1	20	2	1	5							
N ₂ , nuclear coordinate: $n_q = 12, \theta = 35.0$														
distance	1.0	1.5	3.0	4.0	5.0	6.0*	10.0*	15.0*	55.0*					
elements	1	1	10	2	1	1	2	1	4					
NO, electronic coordinate: $n_q = 8, \theta = 35.0$														
distance	1.0	3.0	6.0	10.0	90.0	94.0*	115.0*	195.0*						
elements	1	1	1	1	20	1	3	8						
NO, nuclear coordinate: $n_q = 14, \theta = 45$														
distance	1.0	1.6	9.0	9.25*	10.0*	12.0*	42.0*							
elements	1	1	37	1	1	1	4							
F ₂ , electronic coordinate: $n_q = 12, \theta = 40.0$														
distance	1.5	2.0	4.0	10.0	90.0	110.0*	120.0*	190.0*	500*					
elements	6	1	1	2	20	5	1	4	6					
F ₂ , nuclear coordinate: $n_q = 20, \theta = 35.0$														
distance	1.8	2.0	2.5	2.5969	2.7	10.7	10.8*	11.0*	11.5*	12.5*	14.0*	18.0*	30.0*	101.0*
elements	9	1	5	4	4	4	1	1	1	1	1	1	4	2

- [1] K. Houfek, T. N. Rescigno, and C. W. McCurdy, *Phys. Rev. A* **73**, 032721 (2006).
- [2] K. Houfek, T. N. Rescigno, and C. W. McCurdy, *Phys. Rev. A* **77**, 012710 (2008).
- [3] W. Domcke, *Phys. Rep.* **208**, 97 (1991).
- [4] P. L. Gertitschke and W. Domcke, *Phys. Rev. A* **47**, 1031 (1993).
- [5] B. K. Shandilya, M. Sarma, S. Adhikari, and M. K. Mishra, *Int. J. Quantum Chem.* **113**, 130 (2013).
- [6] R. Čurík and P. Čárský (eds.), *Low-Energy Electron Scattering from Molecules, Biomolecules, and Surfaces* (CRC Press, Boca Raton, 2012).
- [7] A. Herzenberg, *J. Phys. B* **1**, 548 (1968).
- [8] D. T. Birtwistle and A. Herzenberg, *J. Phys. B* **4**, 53 (1971).
- [9] L. Dubé and A. Herzenberg, *Phys. Rev. A* **20**, 194 (1979).
- [10] K. Houfek, M. Čížek, and J. Horáček, *Chem. Phys.* **347**, 250 (2008).
- [11] D. J. Tannor and D. E. Weeks, *J. Chem. Phys.* **98**, 3884 (1993).
- [12] T. N. Rescigno and C. W. McCurdy, *Phys. Rev. A* **62**, 032706 (2000).
- [13] C. W. McCurdy, M. Baertschy, and T. N. Rescigno, *J. Phys. B* **37**, R137 (2004).
- [14] C. W. McCurdy and C. K. Stroud, *Comput. Phys. Commun.* **63**, 323 (1991).
- [15] W. van Dijk and F. M. Toyama, *Phys. Rev. E* **75**, 036707 (2007).
- [16] J. R. Taylor, *Scattering Theory: The Quantum Theory on Nonrelativistic Collisions* (Wiley & Sons, Inc., New York, 1991).
- [17] M. Formánek, M. Váňa, and K. Houfek, *AIP Conf. Proc.* **1281**, 667 (2010).
- [18] See Supplemental Material at <http://link.aps.org/supplemental/10.1103/PhysRevA.95.022714> for videos of the time evolution of the wave packets and the cross sections.
- [19] M. Berman, H. Estrada, L. S. Cederbaum, and W. Domcke, *Phys. Rev. A* **28**, 1363 (1983).
- [20] W. M. Huo, M. A. P. Lima, T. L. Gibson, and V. McKoy, *Phys. Rev. A* **36**, 1642 (1987).
- [21] M. Allan, *J. Phys. B* **18**, 4511 (1985).
- [22] M. Allan, *J. Phys. B* **38**, 3655 (2005).
- [23] C. S. Trevisan, K. Houfek, Z. Zhang, A. E. Orel, C. W. McCurdy, and T. N. Rescigno, *Phys. Rev. A* **71**, 052714 (2005).
- [24] M. Allan, *J. Phys. B* **38**, 603 (2005).
- [25] J. Horáček, M. Čížek, K. Houfek, P. Kolorenč, and W. Domcke, *Phys. Rev. A* **73**, 022701 (2006).